Article

Current Biology

Spontaneous Activity in the Zebrafish Tectum Reorganizes over Development and Is Influenced by Visual Experience

Highlights

- Calcium imaging of zebrafish optic tectum every day from 4 to 9 dpf
- Graph measures derived from spontaneous activity change over development
- Neural assemblies change their properties over development
- Spontaneous activity and behavior are affected by visual experience

Authors

Lilach Avitan, Zac Pujic, Jan Mölter, ..., Rumelo Amor, Ethan K. Scott, Geoffrey J. Goodhill

Correspondence

g.goodhill@uq.edu.au

In Brief

Avitan et al. show that spontaneous activity changes over development in the zebrafish optic tectum, particularly at 5–6 dpf. Graph theoretic analyses reveal corresponding changes in tectal functional architecture. Manipulating visual experience changes both this activity and behavior, demonstrating sensitivity to the structure of visual input.

Avitan et al., 2017, Current Biology *27*, 2407–2419
August 21, 2017 © 2017 Elsevier Ltd.
http://dx.doi.org/10.1016/j.cub.2017.06.056

CellPress

Current Biology
Article

Spontaneous Activity in the Zebrafish Tectum Reorganizes over Development and Is Influenced by Visual Experience

Lilach Avitan,[1] Zac Pujic,[1] Jan Mölter,[1,2] Matthew Van De Poll,[1] Biao Sun,[1] Haotian Teng,[1] Rumelo Amor,[1] Ethan K. Scott,[1,3] and Geoffrey J. Goodhill[1,2,4,*]
[1]Queensland Brain Institute
[2]School of Mathematics and Physics
[3]School of Biomedical Sciences
The University of Queensland, Brisbane, QLD 4072, Australia
[4]Lead Contact
*Correspondence: g.goodhill@uq.edu.au
http://dx.doi.org/10.1016/j.cub.2017.06.056

SUMMARY

Spontaneous patterns of activity in the developing visual system may play an important role in shaping the brain for function. During the period 4–9 dpf (days post-fertilization), larval zebrafish learn to hunt prey, a behavior that is critically dependent on the optic tectum. However, how spontaneous activity develops in the tectum over this period and the effect of visual experience are unknown. Here we performed two-photon calcium imaging of GCaMP6s zebrafish larvae at all days from 4 to 9 dpf. Using recently developed graph theoretic techniques, we found significant changes in both single-cell and population activity characteristics over development. In particular, we identified days 5–6 as a critical moment in the reorganization of the underlying functional network. Altering visual experience early in development altered the statistics of tectal activity, and dark rearing also caused a long-lasting deficit in the ability to capture prey. Thus, tectal development is shaped by both intrinsic factors and visual experience.

INTRODUCTION

The emergence of spontaneous activity is a hallmark of nervous system development, yet its function, developmental trajectory, and susceptibility to disturbances in sensory input are still unclear [1]. The structure of spontaneous activity can give insight into the underlying patterns of brain connectivity [2] and is developmentally altered in disease states such as autism [3]. One suggestion is that it may play the role of a Bayesian prior for expected patterns of sensory activity [4], and indeed patterns of spontaneous activity in cortex are predictive of subsequent patterns of evoked activation across cortical maps [5] (B. Hein et al., 2016, Soc. Neurosci., abstract, program no. 799.11).

Spontaneous activity in the mammalian visual cortex generally takes the form of the sequential activation of neural assemblies, i.e., groups of neurons that tend to fire together [6]. During development this cortical activity is at least partly driven by retinal waves [7], and its statistical structure evolves with time [3, 8]. However, due to the practical limitations of mammalian systems, the early emergence of spontaneous activity across neural populations in the cortex is difficult to study in fine temporal detail. The larval zebrafish provides an ideal model system in this regard, permitting non-invasive imaging of brain activity throughout early development. Zebrafish begin to hunt prey around 5 days post-fertilization (dpf), a behavior that is strongly dependent on their main visual processing center, the optic tectum [9]. Spontaneous retinal waves in zebrafish peak at 3.25 dpf but are largely absent beyond 3.5 dpf [10]. Spontaneous tectal activity at 8 dpf consists of structured neural assemblies, similar to the patterns of activity evoked by prey stimuli at this age [11]. However, how this activity evolves over earlier development is unknown.

Reliable automatic detection of neural assemblies during spontaneous activity is challenging, as these assemblies tend to be very noisy. Each neuron may be part of several assemblies, and the neurons that make up one assembly will not always fire together. Identifying neural assemblies is somewhat analogous to the much better-studied problem of identifying community structure in a network. Graph-theoretic techniques have developed rapidly in recent years, driven by the great interest in mining data from the statistical structure of social networks. These techniques provide powerful new tools that are also applicable to the analysis of neural firing patterns. In particular, very recent work has introduced a new statistical approach for estimating the number of communities in a network [12, 13], which produces excellent performance on benchmark problems [12] but has not yet been applied to finding neural assemblies.

Appropriate visual experience during development is crucial for many aspects of mammalian visual cortical development [14]. In particular, manipulations such as dark rearing during the critical period cause profound changes in the structure of V1 [15]. In contrast, the development of the zebrafish tectum has so far appeared more hard wired, with dark rearing leaving tectal development apparently largely unaffected [16]. Here we systematically mapped how spontaneous activity develops from day to day in the zebrafish tectum during the

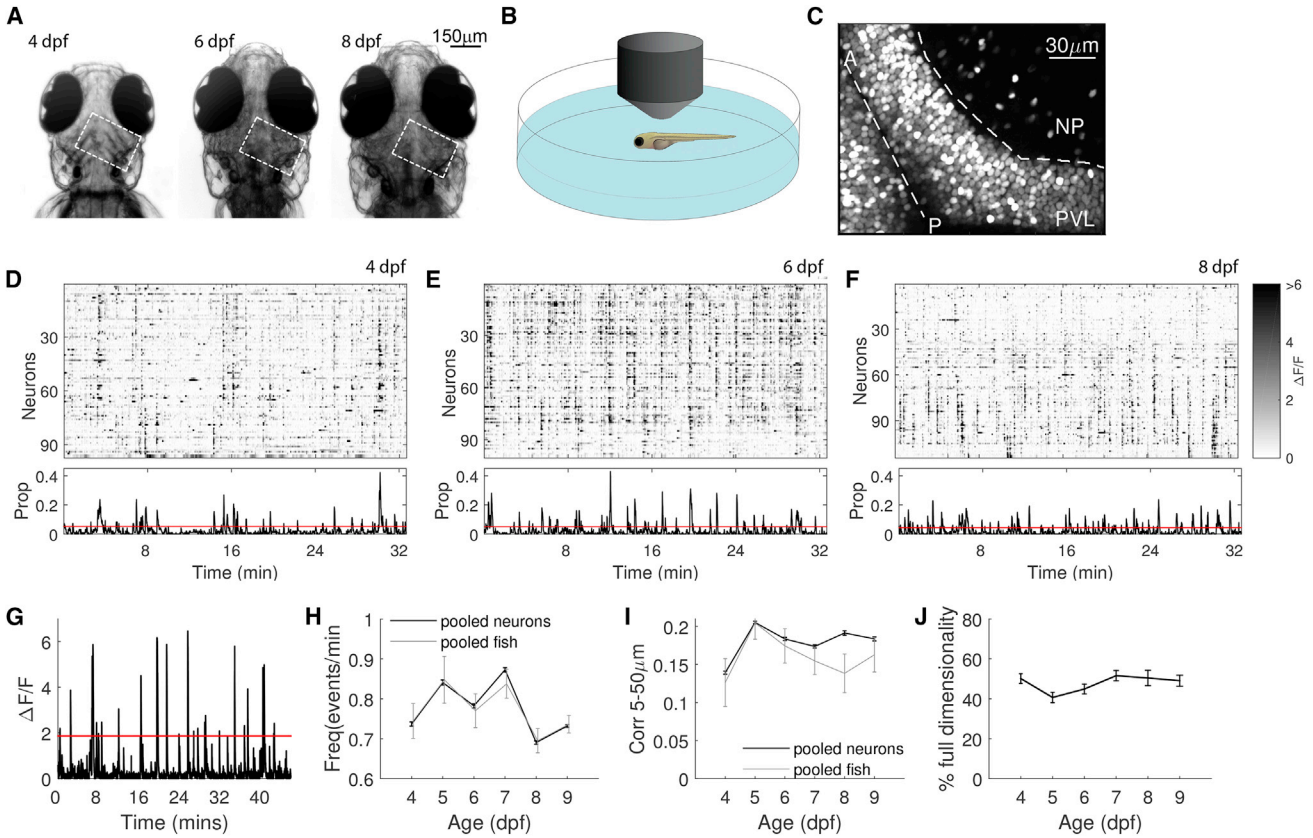

Figure 1. Spontaneous Activity Characteristics Change over Development

(A) A developing larval zebrafish head at 4, 6, and 8 dpf. White dashed rectangle is the imaging area.

(B) Zebrafish embedded in agarose were imaged in the dark using a two-photon microscope for up to 1 hr (schematic not to scale).

(C) Fluorescence image of a 6 dpf tectum expressing H2B-GCaMP6s. PVL, NP, midline (straight dashed line), and anterior (A) and posterior (P) ends of the tectum are indicated.

(D–F) Top: raster plots of spontaneous PVL activity at 4 (D), 6 (E), and 8 dpf (F) revealing sporadic single-neuron activity as well as episodes of synchronous activity. Bottom: proportion of co-active neurons as a fraction of the population recorded for each time bin. The red line indicates the threshold derived from a shuffle control for a statistically significant proportion of co-active neurons in a frame (see STAR Methods).

(G) A $\Delta F/F$ trace of a PVL neuron from a 6 dpf fish. A neuron was considered active if $\Delta F/F$ exceeded two SDs above the mean (red line; see STAR Methods).

(H) Event frequency increases from 4 to 5–7 dpf and then decreases again at 8 and 9 dpf. Mean event frequencies over neurons (black) and fish (gray) follow a similar profile. Error bars are SEM (4 versus 5 dpf, $p = 10^{-4}$; 5 versus 6 and 7 dpf, no difference; 5 versus 8 dpf, $p = 10^{-5}$; 5 versus 9 dpf, $p = 10^{-3}$;4 versus 8 and 9 dpf, no difference; one-way ANOVA over neurons, Bonferroni correction).

(I) Short-range pairwise correlation increases from 4 to 5 dpf. Means over neurons (black) and fish (gray) follow a similar trend (4 versus 5 dpf, $p = 10^{-120}$; 5 versus 6 dpf, $p = 10^{-14}$; 5 versus 7 dpf, $p = 10^{-27}$; 5 versus 8 dpf, $p = 10^{-4}$; 5 versus 9 dpf, $p = 10^{-10}$; 4 versus 6 dpf, $p = 10^{-47}$; 6 versus 7 dpf, no difference; one-way ANOVA over neurons, Bonferroni correction).

(J) Data dimensionality as the percentage of principal components required to explain 80% of the variance in activity shows a dip at 5 dpf (4 versus 5 dpf, $p = 0.02$; 4 dpf versus the rest, no difference; t test).

See also Figure S1.

period 4–9 dpf, using GCaMP6s and two-photon calcium imaging. We characterized the changes in spontaneous activity over development, and we applied graph-theoretic techniques to extract statistical patterns over time from these data, relating to both functional connectivity and neural assemblies. We also investigated how the characteristics of spontaneous activity are perturbed by early eye enucleation, dark rearing, and featureless rearing. Our results reveal profound changes in network organization over this period in zebrafish, identify 5–6 dpf as a critical moment in zebrafish tectal development, and show that changes in visual experience are sufficient to disrupt normal tectal functional architecture and hunting behavior.

RESULTS

Statistics of Tectal Spontaneous Activity Change over Development

To study the statistics of spontaneous activity over development, we performed two-photon calcium imaging of larval zebrafish from 4 to 9 dpf (Figure 1). During this period, zebrafish transition from self-feeding via the yolk sac to feeding via hunting behavior, which is critically dependent on the optic tectum [9]. The tectum is divided into two main areas, the periventricular layer (PVL), which contains the cell bodies of most tectal neurons, and the synaptic neuropil area (NP), which contains their

dendrites and axons, the axons of retinal afferents, and sparsely distributed cell bodies. We used the fluorescent indicator H2B-GCaMP6s, a nuclear-targeted protein that only shows calcium activity in PVL and NP cell bodies and not axons or dendrites in the NP. We recorded from both the PVL and NP for up to 1 hr in the dark from awake larvae embedded in agarose (Figures 1B and 1C) (4 dpf, n = 7 fish, mean 76 neurons/fish; 5 dpf, n = 7 fish, mean 101 neurons; 6 dpf, n = 9 fish, mean 85 neurons; 7 dpf, n = 12 fish, mean 56 neurons; 8 dpf, n = 8 fish, mean 58 neurons; and 9 dpf, n = 8 fish, mean 60 neurons).

Spontaneous activity at all ages was composed of occasional single-neuron calcium transients as well as episodes of synchronous calcium transients across ensembles of neurons (Figures 1D–1F). We first characterized changes over development at the single-cell level. Elevations in calcium signal amplitude were measured as deflections from baseline $(\Delta F/F)$, which we refer to as calcium events (Figure 1G) (see STAR Methods). Surprisingly, the frequency of calcium events of PVL neurons increased from 4 dpf to 5–7 dpf and afterward decreased at 8 and 9 dpf (Figure 1H). Short-range pairwise correlations (5–50 μm) in the tectum peaked at 5 dpf and declined thereafter (Figure 1I). Furthermore, the dimensionality of the data, i.e., the percentage of principal components required to explain 80% of the variance in activity, decreased at 5 dpf, suggesting higher population synchrony at this age (Figure 1J). Thus, the developing tectum exhibits substantial changes in spontaneous activity for both individual neurons and at the population level, suggesting that the circuit is reorganizing during this time.

Two Spatially and Functionally Segregated Populations of NP Neurons

Besides the PVL, some aspects of tectal information processing also involve neurons located in the NP. Superficial layers of the tectal NP receive input from the vast majority of retinal axons. In particular, superficial inhibitory interneurons (SINs) play important roles in filtering out low-frequency spatial information [17], as well as encoding object size [18] and diverse features of looming stimuli [19]. Deep layers of the NP receive input from superficial NP neurons and also a small proportion of retinal input. Information from deep-layer neurons is transmitted to PVL neurons and then sent to premotor areas in the midbrain and hindbrain [20, 21]. We therefore asked whether this functional segregation of NP neurons was reflected in their spontaneous activity patterns and developmental trajectories.

We fitted an ellipse to the NP contour of each fish (Figure S1A) and projected the coordinates of each NP neuron onto the ellipse's major and minor axes, representing the anterior-posterior axis and the latero-medial axis, respectively. In our recordings, NP neurons were fewer in number than PVL neurons, representing less than 15% of the population recorded per fish. At each age, there was no significant correlation between event frequency and position of NP neurons on the anterior-posterior axis. However, there was a significant correlation between event frequency and the depth of NP neurons, i.e., position on the latero-medial axis, for all days except 4 and 9 (Figure S1B). NP neurons closer to the skin showed lower event frequency than deeper NP neurons. The distribution of event frequency of NP neurons was fitted by a Gaussian mixture model (Figure S1C). The distribution was best explained by three Gaussians; however, two of the Gaussians captured most of the data, suggesting two separate populations with different mean event frequencies. These two populations had a clear spatial segregation (Figures S1D–S1F). NP neurons that showed low event frequency (below one event per minute) were more superficial than NP neurons with high event frequency (t test, $p = 10^{-12}$). The event frequency of both of these populations of NP neurons remained constant over development (Figure S1G). Thus, consistent with distinct functional roles in response to visual cues, there are two spatially segregated populations of NP neurons, exhibiting different and developmentally stable patterns of spontaneous activity and a different developmental profile to the PVL neurons.

Graph-Theoretic Analysis Reveals Changes in Functional Network Architecture over Development

A powerful way to describe the functional organization of the tectum is to treat the tectum as a graph, a mathematical structure composed of a set of nodes joined together in pairs by edges [22]. We applied graph-theoretic techniques in two different ways to our data. First, to examine functional connectivity, we constructed a graph for each recorded tectum in which each node represents a neuron and each edge between two neurons represents the correlation between them. A binary connectivity matrix (adjacency matrix) was derived by thresholding this matrix so that only high correlations (≥ 0.3) are represented (Figures 2A–2C). Second, to extract neural assemblies from the movies, we used the approach described in the next section.

The functional connectivity graphs arising from the first approach can be described by a variety of standard metrics, whose changes over development give insight into the functional reorganization taking place. The graph mean degree, i.e., the mean number of neighbors over all nodes, peaked at 5 dpf (Figure 2D), indicating a peak in overall network connectivity at 5 dpf. In contrast, the mean degree of NP neurons showed a slight but non-significant decrease over age (Figure 2E). The degree distribution, $p(k)$, i.e., the fraction of nodes in the graph with degree k followed a power law $p(k) \sim k^{-\alpha}$, $\alpha = 1 \pm 0.1$ in all graphs over development (Figure 2F). This topological feature, often called "scale free," is common to many real world networks [23] and indicates a high proportion of nodes with low connectivity and a low proportion of "hub" nodes with higher connectivity than expected by chance. We also investigated measures of segregation that quantify the presence of densely interconnected groups of nodes in the graph, known as communities [24]. A simple measure of segregation is the clustering coefficient [25]. This is based on the fraction of triangles around an individual node, i.e., the fraction of the node's neighbors (defined by graph edges) that are also neighbors of each other and reflects the prevalence of clustered connectivity around individual nodes. The mean clustering coefficient increased from 4 to 5 dpf and then decayed and remained stable (Figure 2G). For comparison, we generated an equivalent set of 40 random (Erdős-Rényi) graphs per fish, which maintained the number of nodes and edges, but the edges were placed randomly. The mean clustering coefficient in the equivalent random graphs was substantially lower and remained stable over development (Figure 2G). Thus, the tectal graphs were more clustered than expected by chance at all ages but were most clustered at 5 dpf.

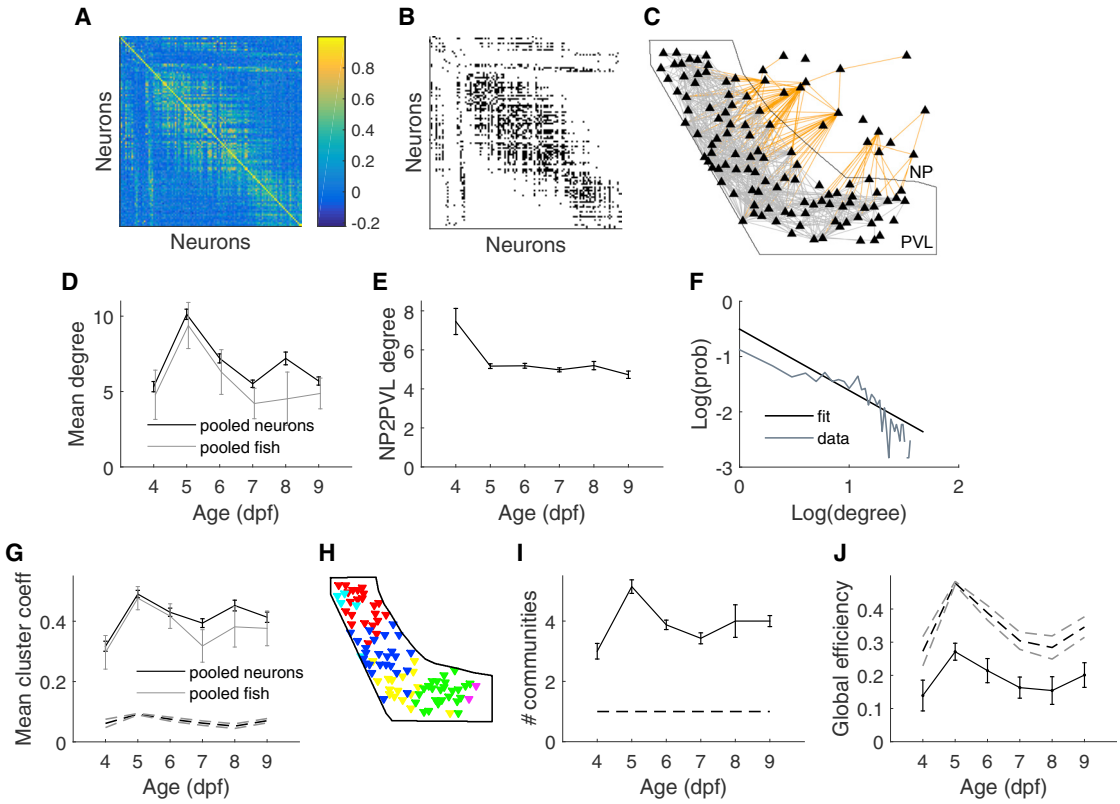

Figure 2. Graph Measures Reveal Changes in Functional Network Architecture over Development

(A) Neuron-to-neuron correlation matrix of a 6 dpf fish.

(B) Thresholded correlation matrix, providing an adjacency matrix for graph construction.

(C) A representation of the tectum as a graph. Each node (triangle) represents a neuron, and each edge represents functional connectivity between two neurons (gray lines for intra-PVL edges and orange lines for edges involving NP neurons). The solid black outline shows the boundary of the PVL.

(D) Mean graph degree over development increases from 4 dpf to 5–6 dpf and then decreases at 7–9 dpf. Mean degree over neurons (black) and fish (gray) follow a similar profile (4 versus 5 dpf, $p = 10^{-24}$; 4 versus 6 dpf, $p = 10^{-3}$; 4 versus 7 dpf, no difference; 5 versus 6 dpf, $p = 10^{-10}$; 5 versus 7 dpf, $p = 10^{-25}$; 5 versus 8 dpf, $p = 10^{-8}$; 5 versus 9 dpf, $p = 10^{-20}$; one-way ANOVA over neurons, Bonferroni correction).

(E) The NP-to-PVL mean degree shows a slight but non-significant decrease over development.

(F) Degree distribution probability of 6 dpf fish (gray) and the fitted power law curve (black) plotted on a log scale suggest that the graph topology is scale free. Other days are very similar.

(G) Mean clustering coefficient increases at 5 dpf and then decreases at 6 and 7 dpf. Mean clustering coefficient over neurons (black) and fish (gray) follow a similar profile. (4 versus 5 dpf, $p = 10^{-14}$; 5 versus 6 dpf, $p = 0.03$; 5 versus 7 dpf, $p = 10^{-4}$; 5 versus 8 dpf, no difference; 5 versus 9 dpf, $p = 10^{-3}$; 4 versus 6 dpf, 10^{-5}; 6 versus 7 dpf, no difference; one-way ANOVA, Bonferroni correction). The clustering coefficient for the equivalent random (Erdős-Rényi) graphs is stable over development (mean, dashed black line; SEM, dashed gray line).

(H) Six communities (color coded) were detected in the graph presented in (C).

(I) The number of communities peaks at 5 dpf (4 versus 5 dpf, $p = 0.03$; 5 versus 6 dpf, no difference; 5 versus 7 dpf, $p = 0.04$; t test). Only graphs with more than 20 connected PVL neurons were considered for community structure analysis. The equivalent random (Erdős-Rényi) graphs are stable at one community over development (dashed black line).

(J) Global efficiency peaks at 5 dpf, indicating an increase in short-range functional connections at 5 dpf. The global efficiency for the equivalent Erdős-Rényi graphs is higher (mean, dashed line; SEM, gray line) (4 versus 5 dpf, $p = 0.03$; 5 versus 6 dpf, no difference; 5 versus 7 dpf, $p = 0.03$; 4 versus 6 dpf, no difference; t test).

We also looked at measures of functional integration, which estimate the ease with which nodes communicate. These are based on the concept of a path, i.e., sequences of distinct nodes and edges representing routes of information flow between pairs of nodes. The lengths of the paths consequently estimate the potential for functional integration between nodes, with shorter paths implying stronger potential for integration. Global efficiency, which is the average inverse shortest path length, peaked at 5 dpf (Figure 2J). When compared with equivalent Erdős-Rényi graphs, we found higher global efficiency in the latter, consistent with higher values of global efficiency in random graphs relative to scale-free graphs.

However, more sophisticated measures of segregation in a graph have recently been developed, which find the number of densely interconnected groups of nodes and their composition, i.e., community structure. While various heuristic algorithms exist, more mathematically rigorous approaches have been based on statistical inference. The observed network is fitted

to a general class of models by adjusting the parameters of the model, and the parameters then provide information about the structure of the network. The most common model in this context is the stochastic block model [26]. Graphs within the model arise by assigning n nodes to k communities randomly and then assigning edges between pairs of nodes with a probability that depends on whether or not the nodes are in the same community. The probability that the observed graph was constructed from these parameters can then be determined. By applying Bayes theorem, the posterior distribution over k and all possible assignments can then be calculated, i.e., the likelihood of each value of k and an assignment given the observed graph, and some assumption about the prior distribution over k (usually taken to be uniform, i.e., all values of k from 1 to n are equally likely). We employed a very recent development of this approach, which uses the degree-corrected stochastic block model [12] (see STAR Methods). This is both computationally efficient and has been shown to have excellent performance on benchmark problems. Having determined the number of communities, we then used a standard spectral clustering approach [13, 27] to assign nodes to these communities (see STAR Methods) (Figure 2H). The mean number of communities increased from 4 to 5 dpf, after which it decayed and remained stable (Figure 2I). Thus, although the underlying topology of the network remains robust, tectal functional connectivity refines over development.

Changes in Concerted Spontaneous Activity over Development

Spontaneous activity at all ages was characterized by concerted activity over assemblies of neurons, i.e., time points (frames), including a number of co-active neurons that exceeded the number expected to be co-active by chance (Figures 1D–1F). We asked whether the overall activity for each fish could be well characterized by a small number of neural assemblies that repeated over the recording. This is a challenging problem for two reasons. First, the number of assemblies present is unknown a priori. Second, such assemblies are inherently noisy, with each neuron potentially belonging to more than one assembly and not necessarily firing reliably every time its associated assembly is active. While a number of different approaches to this problem have been proposed (e.g., [28–30]), we used graph-theoretic techniques utilizing the statistically rigorous stochastic block model algorithm described above. We first illustrate the steps involved for an artificial example. In this context, the graph nodes now represent movie frames rather than neurons, and the goal is to find communities of similar frames within a movie (Figure 3A). That is, rather than taking the correlation between each pair of neurons over the movie as the metric of similarity in the graph, now we consider the similarity in activity pattern between each pair of frames. Assembly instances were identified as densely connected subgraphs. Taking the peak of the probability distribution over the number of communities (Figure 3B), we again used a standard spectral clustering method to divide the graph into this number of densely connected subgraphs [13]. We defined "core" assemblies as the average of the frames within each subgraph, excluding neurons with very low affinity to the assembly (see STAR Methods) (Figure 3C).

Since these techniques have not previously been applied to finding neural assemblies, we first validated them on surrogate data with some of the statistical properties of the real data, but where the ground truth assembly structure was known (see STAR Methods). Unlike the example shown in Figures 3A–3C, the surrogate data contained assemblies that overlapped (see STAR Methods), making their detection a much harder problem. Nevertheless, the graph algorithm still performed well, and in particular better than a recently proposed independent component analysis (ICA)-based technique [29] (Figure 3D; Figure S2). This gave us confidence that the results for real data, where no ground truth is available for reference, were meaningful.

We then applied the same technique on the spontaneous activity data from our fish and obtained a distribution of the potential number of embedded assemblies (Figure 3E). Based on this distribution, we collected similar frames forming a community of frames (Figure 3F; see STAR Methods) and, thus, the core assemblies for each fish (Figure 3G). We then asked whether all assemblies were equally likely to appear. We found that for 47 out of 51 fish, the distribution of assembly frequencies was not significantly different from a uniform distribution. We also analyzed the cohesiveness of the assemblies, i.e., the strength of the coupling between an assembly A and the assembly core neurons n_i that A contains. Given an assembly A, we calculated the mean affinity of neurons, which approximates the average $P(n_i \mid A)$ over all neurons n_i. This measures how likely each neuron is to be active, given that a particular assembly to which the neuron belongs is active. Across assemblies this average ranged between 0.4 and 0.9, with an average over all assemblies for all fish of 0.6. Thus, when an assembly A is active, the neurons that make up its core are also likely to be active. We also looked at $P(A|n_i)$, which measures how likely an assembly is to be active given that a particular assembly neuron is active. For each assembly, we calculated its maximum value over all assembly neurons and then looked at the distribution of these maximum values over all assemblies. Only 4% of these values were above 0.2, with an average over all assemblies of 0.09 ± 0.06 and a maximum of 0.33. Thus, when any particular neuron is active, there is only a relatively small chance that the assembly/assemblies of which it is a part will also be active. This indicates an absence of "driving" neurons, whose activity strongly predicts the behavior of an entire assembly. These two conditional probabilities are quite different due to the fact that each individual neuron is active far more often than any of the assemblies of which it is a member.

To address how the properties of spontaneous neural assemblies change over development, we computed core assemblies for all fish at all ages. The number of assemblies increased from 4 to 6 dpf (Figure 3H), and the number of neurons per assembly peaked at 5 dpf (Figure 3I). The average spatial spread of each cluster, as measured by the area of the smallest ellipse containing the locations of all core neurons in the cluster, decreased with age (Figure 3J) and was significantly lower at 9 dpf than at 4 dpf. Interestingly, despite the increase in number of assembly neurons between 4 and 5 dpf, the area covered by the assembly remains similar. This indicates spatially spread assemblies that are sparser at 4 dpf and denser at 5 dpf. Thus, the properties of assemblies are dynamic over development, gradually becoming

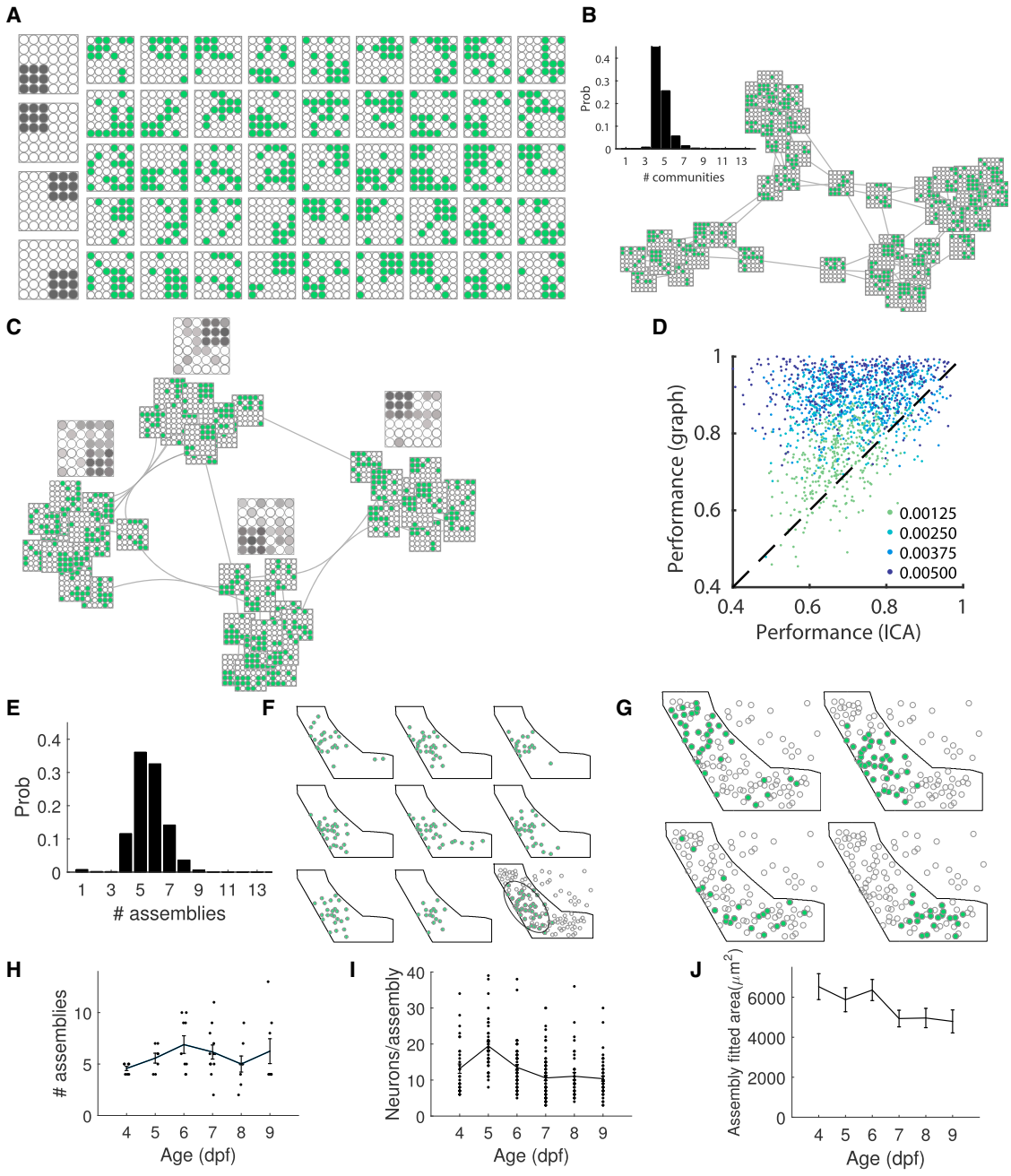

Figure 3. Concerted Spontaneous Activity Changes over Development

(A) An artificial example of assembly reconstruction. Left: four core assemblies were embedded in a population of 36 neurons. Dark circles represent assembly neurons and white circles represent other neurons. Right: all 45 randomly generated frames that were input to the algorithm. Green circles show active neurons and white circles show other neurons.

(B) Spontaneous frames arranged in a k-nearest-neighbor graph according to the frames' cosine similarity measure (spring-electrical embedding visualization [31]). Inset: probability distribution over the number of potential communities embedded in this artificial dataset as determined by the stochastic block model. This peaks at four embedded assemblies.

(C) Division of the graph in (B) using spectral clustering, with each of the clusters identified by its average activity pattern (gray frames, where lighter colors represent weaker affinity to the assembly).

(D) Performance comparison between the graph approach and an alternative ICA-based technique in terms of best match score (see STAR Methods) shows that the graph approach produces more accurate results. This result is robust over different assembly mean frequencies (proportion of active frames, color coded).

(E) Example of application to real data. The probability distribution over the potential number of assemblies peaks at five for the example fish shown in Figure 2.

(F) Highly similar frames defining a core assembly. Each green circle (now binary scale) represents an active cell. Right bottom: the core assembly is the average of highly similar frames (excluding neurons with <20% affinity to the assembly). Also shown is the ellipse fitted to determine the spatial extent of the cluster.

(G) Four core assemblies estimated after optimization, arranged by spatial organization along the anterior-posterior axis.

(legend continued on next page)

more compact, but with the neurons per assembly and number of assemblies peaking at days 5 and 6, respectively.

Enucleation Preserves Some Features of Spontaneous Activity but Disrupts Others

Spontaneous retinal waves are present in many species [32] and play a crucial role in the refinement of visual topographic maps [7, 33–35]. In the developing zebrafish, spontaneous retinal waves are present from 2.5–3.5 dpf [10]. To test whether retinal activity (both evoked and spontaneous) plays a role in the development of spontaneous activity in the tectum, we performed enucleation at 24 hr post-fertilization (hpf) and then recorded spontaneous tectal activity for 1 hr at 6 dpf. We investigated both bilateral (n = 9 fish, mean 32 neurons/fish) and unilateral (n = 10 fish, mean 62 neurons/fish) enucleation, the latter to test whether normal input to an intact tectum influences the development of its fellow denervated tectum. In this case, following imaging of the denervated tectum, the intact tectum was then imaged for 1 hr as an internal control (Figure 4A).

Even after removal of both eyes (bilateral enucleation [BE]), the tectum still showed spontaneous activity, suggesting that this is at least partially driven endogenously. In particular, there were no differences at the single-cell level found between normally reared (NR, n = 8, mean 44 neurons/fish) and BE fish. This was not the case for the unilateral enucleation, where a paired comparison was made between the denervated (Den) tectum and the intact tectum. We found lower event frequency for PVL neurons and a higher proportion of frames with no or only one active neuron in the Den tecta (Figures 4B and 4C). Intriguingly, however, at a population level the intact tecta in the unilateral enucleation case showed statistics much more similar to the Den and BE tecta than to the tecta of NR fish, indicating a role for interhemispheric transfer of information to the Den tectum. In particular the Den, BE, and intact tecta were all more correlated than NR tecta at most distances, though the intact tecta were most similar to the NR case (Figure 4D). This pattern was also reflected in the mean graph degree (Figure 4E). Spontaneous neural assemblies were still present in the Den, BE, and intact tecta, though they were slightly fewer in number (Figure 4F). Neurons per assembly were lowest for the NR case (Figure 4G), and assembly area was similar across the different cases (Figure 4H). Neuron position in the tectum was more correlated with assembly center of mass in the NR and intact tecta compared to the Den and BE tecta (Figure 4I). Similar to the NR case, all assemblies were equally likely to appear, and in only two fish was the distribution of assembly frequencies different from a uniform distribution. The affinity between neurons and assemblies was also similar to the NR case. Thus, tectal spontaneous activity is at least partially driven by non-retinal sources and influenced by interhemispheric transfer, but retinal input during development still plays an important role in shaping the statistics of spontaneous activity in the tectum.

Dark Rearing Influences the Spatial Structure of Population Activity and Prey-Capture Performance in a Behavioral Assay

To directly address the influence of spontaneous retinal activity on tectal development, we reared larvae in the dark starting from 5 to 8 hpf and imaged tectal spontaneous activity at 6 dpf (n = 8 fish, mean 65 neurons/fish). Similar to the BE case, single-cell statistics in the dark-reared (DR) fish were largely the same as the NR 6 dpf fish (n = 9 fish, mean 85 neurons/fish) (10/14 hr dark-light cycle). In particular, there were no significant differences in PVL neuron event frequency distributions (Figure 5A). This is consistent with earlier work showing no difference in single-cell visual response properties between DR and NR fish [16]. There was a slight difference in event frequency of NP neurons (Figures 5B and 5C), consistent with an earlier report of changes in NP due to dark rearing [36]. Slight differences were observed in correlation structure between NR and DR. Pairwise correlations were lower at short range (up to 50 μm) in the DR case (Figure 5D). Interestingly, this is in the opposite direction from the increase in correlation caused by enucleation.

There were, however, substantial changes in the higher-order properties of spontaneous activity in DR versus NR fish. Functional connectivity as measured by graph statistics was different in DR compared to NR fish. Graphs for the DR fish had a lower mean degree (Figure 5E) and lower clustering coefficients (Figure 5F), although the network topology remained scale free (Figure 5G). DR fish also had lower numbers of assemblies (Figure 5H), although there was no difference in the number of neurons per assembly or the assembly area compared to normal fish (Figures 5I and 5J). Similar to NR fish, assemblies were equally likely to appear, and for only one DR fish was the distribution of assembly frequencies significantly different from a uniform distribution. Again the affinity between neurons and assemblies was similar to the NR case. Thus, whereas examining only first-order statistics of spontaneous activity suggests that dark rearing has no effect, a significant impact of dark rearing is revealed by examining pairwise correlations. Short-range correlations decrease, neurons have fewer functional connections, these connections are less clustered, and the number of assemblies decreases.

Dark rearing alters the statistics of tectal spontaneous activity, but does it also alter visually guided behavior? To test this, we placed DR and clutch-mate NR fish individually in 35 mm dishes with 50 *Paramecia* and then 2 hr later counted how many *Paramecia* remained uneaten in each dish (see STAR Methods). At 6 dpf, on the first exposure of both NR and DR fish to food they had to hunt, NR fish (n = 12) consumed many more *Paramecia* than DR fish (n = 18) (Figure 5K). Both sets of fish were then fed once per day with rotifers and *Paramecia* and assayed again at 9 dpf. Remarkably, while DR fish (n = 16) had improved slightly, they still did not hunt as effectively as NR fish (n = 14). Thus, besides altering tectal activity

(H) The number of assemblies increases from 4 to 6 dpf ($p = 0.03$, t test). Error bars are SEM.
(I) The number of neurons per assembly peaks at 5 dpf and remains stable between 6 and 9 dpf (4 versus 5 dpf, $p = 10^{-3}$; 5 versus 6 dpf, $p = 10^{-4}$; 5 versus 7 dpf, $p = 10^{-6}$; 5 versus 8 dpf, $p = 10^{-4}$; 5 versus 9 dpf, $p = 10^{-7}$; 4 versus 6–9 dpf, no difference; one-way ANOVA, Bonferroni correction). Error bars are SEM.
(J) The assembly-fitted ellipse area (measured in μm^2) decreases over development, indicating that assemblies gradually change their spatial properties (4 versus 9 dpf, $p = 10^{-2}$, Wilcoxon rank-sum test). Error bars are SEM.
See also Figure S2.

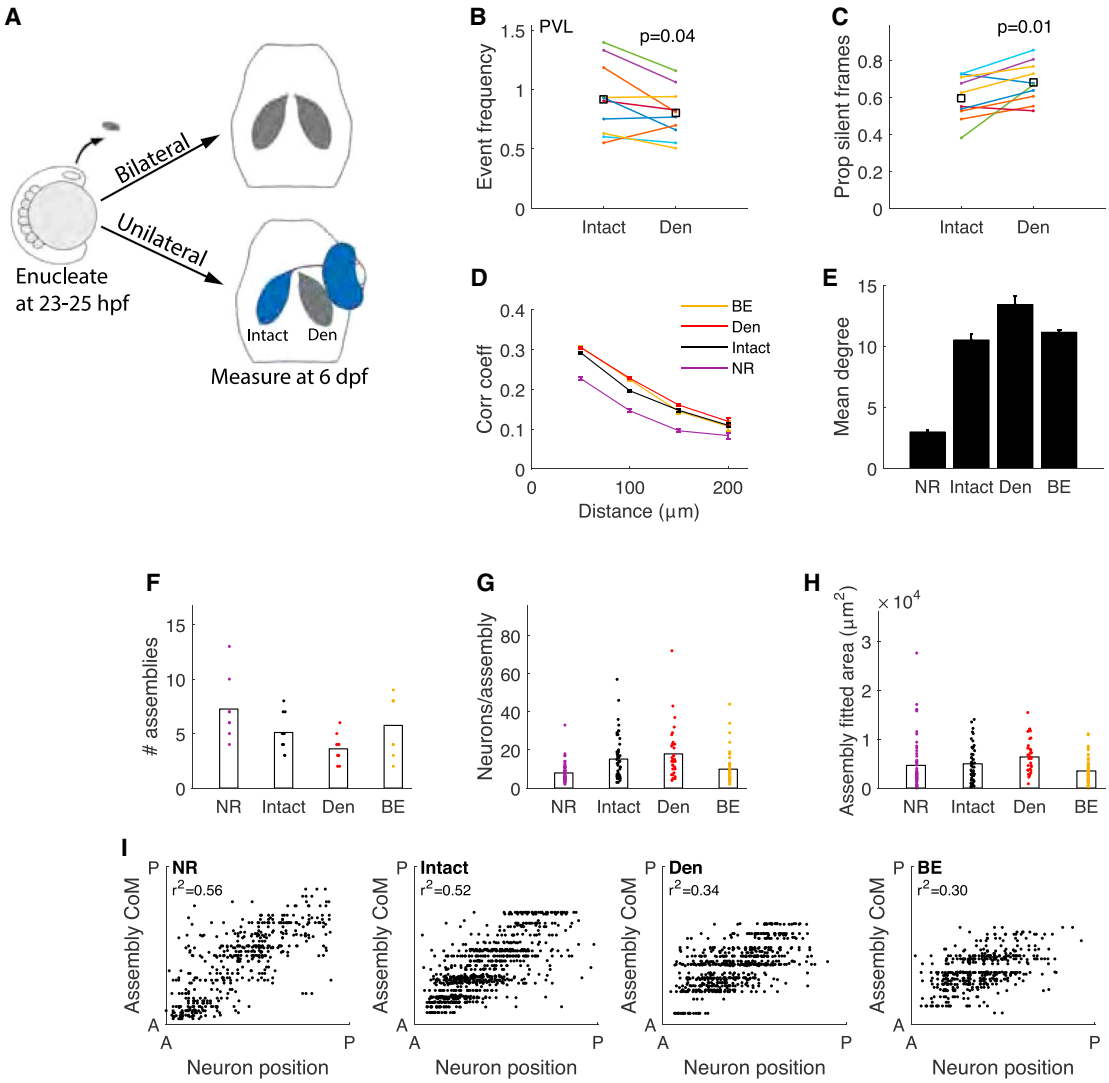

Figure 4. Enucleation Changes Spontaneous Activity Statistics

(A) Experimental procedure for 24 hr enucleations. Larvae at 23–25 hpf were anesthetized and enucleated unilaterally or bilaterally. Fish were then imaged for spontaneous activity at 6 dpf. Denervated (Den) and intact tecta were imaged for 1 hr each (n = 10 fish). Bilaterally enucleated (BE) fish (n = 9) were compared with normally reared (NR) fish (n = 8).

(B) Event frequency of PVL neurons in the unilateral case is lower in the Den than the intact tecta (paired t test).

(C) The number of low-activity frames (one or zero neurons active) is higher in the Den tectum.

(D) Den, intact, and BE tecta are more correlated than NR tecta (NR versus BE, $p = 10^{-48}$, $p = 10^{-40}$, $p = 10^{-7}$, and no difference; NR versus Den, $p = 10^{-69}$, $p = 10^{-63}$, $p = 10^{-25}$, and $p = 10^{-2}$; NR versus intact, $p = 10^{-60}$, $p = 10^{-34}$, $p = 10^{-16}$, and $p = 10^{-2}$; for 0–50, 50–100, 100–150, and 150–200 μm, respectively). Error bars are SEM.

(E) Graph mean degree is higher in the Den, intact, and BE tecta than the NR tecta (intact versus Den, $p = 10^{-2}$; intact versus NR, $p = 10^{-17}$; intact versus BE, no difference; Den versus NR, $p = 10^{-30}$; Den versus BE, no difference; NR versus BE, $p = 10^{-14}$; one-way ANOVA, Bonferroni correction). Error bars are SEM.

(F) The number of assemblies is lower in the Den than the intact tectum or NR tectum ($p = 0.05$ and $p = 10^{-3}$, respectively, Wilcoxon rank-sum test). Number of assemblies in the NR fish is not different from the BE fish.

(G) Den and intact tecta have a similar number of neurons per assembly, higher than the number of neurons per assembly in NR fish. There is no difference between NR and BE tecta (intact versus NR, $p = 10^{-3}$; Den versus NR, $p = 10^{-5}$; Den versus BE, $p = 10^{-3}$; Kruskal-Wallis nonparametric one-way ANOVA, Bonferroni correction).

(H) Den assemblies cover greater area than the NR or the BE assemblies (Den versus NR, $p = 10^{-2}$; Den versus BE, $p = 10^{-3}$; intact versus Den, no difference; Kruskal-Wallis nonparametric one-way ANOVA, Bonferroni correction).

(I) Spatial relation between assembly neurons and assembly center of mass suggests that NR and intact assemblies are sparser and more compact than Den and BE assemblies.

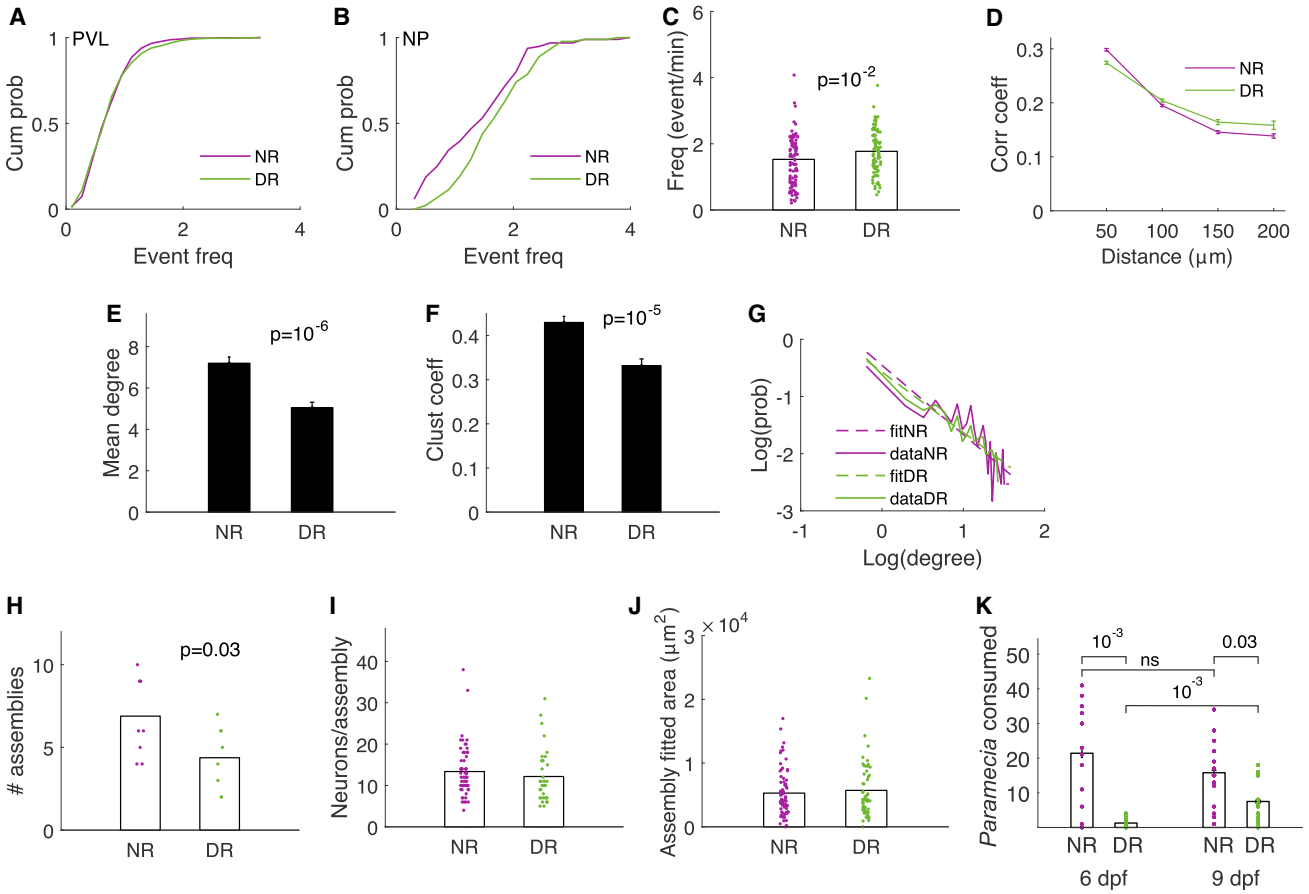

Figure 5. Dark Rearing Changes Local Circuit Properties and Behavior

(A) Dark-reared (DR) and NR PVL event frequency distributions are similar (Kolmogorov-Smirnov test), suggesting no difference at the single-cell level.

(B) DR and NR NP event frequency distributions are different ($p = 0.004$, Kolmogorv-Smirnov test).

(C) DR NP mean event frequency is higher than NR (t test).

(D) Correlation coefficients for PVL neurons show a slightly different profile with distance (0–50 μm, $p = 10^{-13}$; 50–100 μm, no difference; 100–150 μm, $p = 0.01$; 150–200 μm, no difference; Wilcoxon rank-sum test). Error bars are SEM.

(E) DR functional connectivity graphs have lower mean degree (t test). Error bars are SEM.

(F) DR graphs have lower cluster coefficient than NR graphs (t test). Error bars are SEM.

(G) The network topology remains a scale-free network (NR, $\alpha = 1.1$; DR, $\alpha = 1$).

(H) Fewer assemblies are detected in DR fish than in NR fish (t test).

(I) Assemblies detected in both conditions (NR and DR) have the same mean number of neurons per assembly.

(J) Assemblies detected in both conditions (NR and DR) cover the same area.

(K) DR fish consumed fewer Paramecia compared to NR fish of the same age (6 dpf) when both were first introduced to food. DR fish, which were subsequently exposed to light from 6 to 9 dpf, still showed a deficit in feeding behavior compared to the NR fish of the same age (9 dpf) (Wilcoxon rank-sum test, Benjamini Hochberg multiple comparison correction).

patterns, DR has a profound and long-lasting effect on subsequent hunting ability, suggesting a strong effect of visual experience on visually guided behavior.

Patterned Visual Input Is Required for Normal Tectal Development

Is merely the presence of light input required for normal tectal development, or is the spatial structure of the environment also important? To test this, we reared fish on a normal light-dark cycle but in a featureless visual environment (featureless rearing [FR]), with no visual contours or edges (see STAR Methods) and imaged at 6 dpf (n = 9 fish, mean 34 neurons/fish). Event frequencies in both the PVL and NP were unchanged, as were the number of assemblies, the number of neurons per assembly, and the assembly area. However, FR caused an increase in correlations between neurons (Figures 6A and 6B), consistent with the changed structure of the visual environment. Mean degree and local clustering also increased (Figures 6C and 6D), but the network topology remained scale free (Figure 6E). Assembly frequencies and affinities were similar to the NR case. We performed the same prey-capture assay as for the DR fish, but we found no difference in feeding performance with NR fish at 6 dpf (n = 14 FR fish and n = 30 NR fish). Thus, while the effect of FR was more subtle than DR, a lack of visual contours during development did cause measurable changes in the tectal functional network.

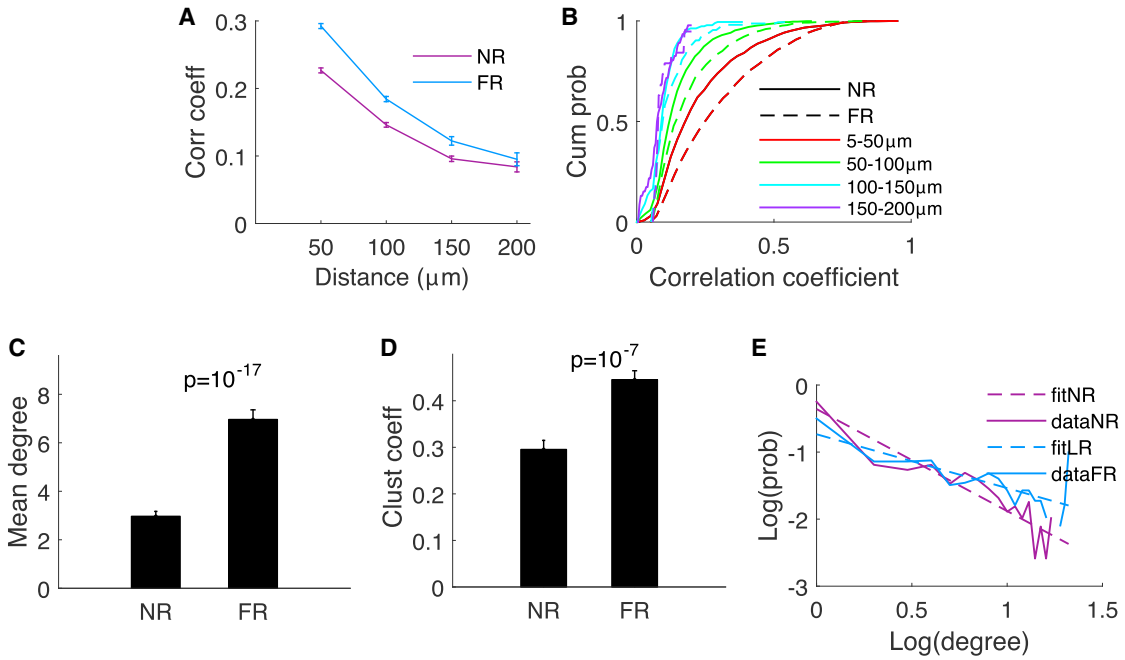

Figure 6. Featureless Rearing Changes Local Circuit Properties

(A) Correlation coefficients for PVL neurons are higher in FR relative to NR fish. Error bars are SEM.

(B) Cumulative distributions of correlation coefficients show a difference in correlations between NR (solid line) and FR (dashed line) fish at most distances (0–50 μm, $p = 10^{-38}$; 51–100 μm, $p = 10^{-10}$; 101–150 μm, p = 0.02; 151–200 μm, no difference; Kolmogorov-Smirnov test).

(C) FR functional connectivity graphs have higher mean degree (t test). Error bars are SEM.

(D) FR graphs are more locally clustered than NR graphs (t test). Error bars are SEM.

(E) The network topology remains a scale-free network (NR, $\alpha = 1.5$; FR, $\alpha = 0.8$).

DISCUSSION

The development of tectal functional properties could, in principle, be driven by changes in feedforward connections from the retina, changes in intratectal connections and/or intrinsic tectal cell properties, or both. Axons from the retina first arrive in the tectal NP at 2 dpf, and from 2 to 4 dpf they navigate to their topographically appropriate targets using a biased branching mechanism [37, 38]. Retinal axon arbors increase in total length and number of branches from 3 to 6 dpf and then stabilize [39]; during this period, the dendrites of tectal neurons also increase their total arbor length [40]. This is temporally consistent with the peak in several measures related to spontaneous activity that we observed at 5–6 dpf. Although subsequent anatomical pruning of axonal and dendritic arbors has not been observed, arbor refinement via functional synaptic elimination could potentially contribute to the decline we observed after 5–6 dpf.

Little is known about either the detailed structure or developmental trajectory of intratectal connections in zebrafish. In *Xenopus* larvae, intratectal connections play an important role in sensory processing, which depends on an appropriate balance of excitation and inhibition [41]. Furthermore, refinement of local tectal circuits occurs over *Xenopus* development, leading to functional changes [42, 43]. Recent work has found a transient increase in tectal neuron excitability at stage 47, when the larvae are 5 days old, perhaps indicating a critical moment in *Xenopus* tectal development [44]. These findings are consistent with our own in zebrafish and argue that developmental changes within the tectum, not just changes in feedforward input, are also likely to contribute to the observed temporal changes in tectal spontaneous activity.

The development of receptive field properties in the zebrafish tectum [45] shows a similar trajectory to our observations of spontaneous activity. In particular, receptive field size increases from 4 to 6 dpf and then refines to the same size as that at 4 dpf by 8–9 dpf, with the excitatory components of the receptive field playing a larger role in determining this developmental profile than the inhibitory components. During this period, GABAergic responses most likely switch from depolarizing to hyperpolarizing [45]. Overall, these authors concluded that functional pruning of feedforward inputs is the most important factor in receptive field refinement. Taken together, the above results from zebrafish and *Xenopus* suggest that changes in both feedforward and intratectal connectivity contribute to the developmental trajectory of spontaneous activity.

Dark rearing has previously been reported to have little or no effect on zebrafish tectal development [16, 21, 36, 46–49]. In contrast, we found that dark rearing increased tectal event frequency of NP cells, reduced the mean degree and cluster coefficient of the tectal functional network, reduced the number of neural assemblies present, and had a long-term impact on the ability to hunt prey (Figure 5). Thus, despite the lack of obvious changes in morphology or receptive fields, the absence of normal visual input during development did have an effect on both behavior and the higher-order statistical properties of functional networks in the tectum. This suggests that the statistics of spontaneous

retinal activity do not entirely mimic those of the natural scenes that zebrafish larvae normally encounter [4, 50–52].

Although at the single-cell level no differences were found between BE fish and NR fish, at the population level both bilateral and unilateral enucleation caused substantial changes in correlation structure, and pairwise correlations in both the BE tecta and Den (unilateral case) tecta were higher than in NR tecta (Figure 4). This could be explained by analogy with data from mice, where eye opening normally leads to "sparsification" of cortical activity whereby neurons become less synchronized [53]. Such sparsification could lead to the drop in short-range correlation we observed after 5 dpf (Figure 1I). By contrast, in our enucleated zebrafish, there was a lack of the input activity needed to drive sparsification of tectal activity. Interestingly, correlation structure in the intact tectum resembled that in BE and Den tecta more than the NR tecta, indicating a role for interhemispheric connections in transmitting information between the hemispheres. Remarkably, in the unilateral case, Den tecta had a much greater impact on the intact tecta than the other way around.

While our paper was in review, a paper was published that also looked at the development of spontaneous activity in the zebrafish tectum (using GCaMP3) and the effect of binocular enucleation [54]. While our findings are broadly in agreement with this work, we also make several new contributions. Most importantly, these include the graph-theoretic analysis of changes in functional connectivity over development, a new graph-theoretic approach to finding assemblies, and the demonstration that both enucleation and more subtle manipulations of visual experience cause significant changes in both the development of spontaneous activity and, for dark rearing, prey-capture ability.

The zebrafish tectum has conventionally been thought of as a relatively hard-wired structure, following intrinsic rules of development driven primarily by cues such as molecular gradients. Here we have shown that its functional architecture does not develop in a smooth and monotonic fashion, but rather has a specific developmental trajectory with a peak in many measures occurring at 5–6 dpf. Furthermore, its network organization is dependent on the statistical structure of retinal activity and is sensitive even to the statistical differences between natural scenes and retinal spontaneous activity. An intriguing possibility is that 5–6 dpf of zebrafish tectal development can be thought of as a "critical period," analogous to the well-documented critical periods in the development of mammalian cortex [55]. An exciting avenue for future work is to explore the effect on zebrafish tectal development of the kind of manipulations of both visual input and pharmacology that have been performed during the critical period in mammals [56]. The zebrafish's rapid development and relative ease of manipulation could potentially allow more rapid exploration of disorders of the critical period than is possible in mammalian systems, thus facilitating the development of new treatments.

STAR★METHODS

Detailed methods are provided in the online version of this paper and include the following:

- KEY RESOURCES TABLE
- CONTACT FOR REAGENT AND RESOURCE SHARING
- EXPERIMENTAL MODEL AND SUBJECT DETAILS
  - Zebrafish
- METHOD DETAILS
  - Dark rearing (DR)
  - Enucleations at 24 hpf
  - Featureless-rearing (FR)
  - Feeding assay
  - 2-photon calcium imaging
  - Image registration
  - Cell detection and calcium signals
  - Calcium events
  - Determination of a statistically significant level of co-activity
  - Significance of pairwise correlation coefficients
  - Estimating the number of communities in the graph
  - Community structure assignment
  - Assembly detection
  - Evaluating the performance of assembly detection
- QUANTIFICATION AND STATISTICAL ANALYSIS
  - Statistical correction for multiple comparisons
- DATA AND SOFTWARE AVAILABILITY
  - Software

SUPPLEMENTAL INFORMATION

Supplemental Information includes two figures and can be found with this article online at http://dx.doi.org/10.1016/j.cub.2017.06.056.

AUTHOR CONTRIBUTIONS

Conceptualization, L.A. and G.J.G.; Methodology, L.A., Z.P., J.M., R.A., and G.J.G.; Software, L.A., J.M., and H.T.; Investigation, L.A., Z.P., B.S., and M.V.D.P.; Resources, G.J.G. and E.K.S.; Writing – Original Draft, L.A., J.M., and G.J.G.; Writing – Review & Editing, L.A., Z.P., J.M., M.V.D.P., B.S., H.T., R.A., E.K.S., and G.J.G.; Supervision, G.J.G. and E.K.S.; Funding Acquisition, G.J.G.

ACKNOWLEDGMENTS

We thank Misha Ahrens for the *elavl3:H2B:GCaMP6s* transgenic line. This work was funded by the Australian Research Council (grant DP150101152). Imaging was performed at the Queensland Brain Institute's Advanced Microscopy Facility and funded by the Australian Government through the ARC LIEF grant LE130100078.

Received: December 29, 2016
Revised: May 18, 2017
Accepted: June 20, 2017
Published: August 3, 2017

REFERENCES

1. Ringach, D.L. (2009). Spontaneous and driven cortical activity: implications for computation. Curr. Opin. Neurobiol. *19*, 439–444.
2. van den Heuvel, M.P., and Hulshoff Pol, H.E. (2010). Exploring the brain network: a review on resting-state fMRI functional connectivity. Eur. Neuropsychopharmacol. *20*, 519–534.
3. Gonçalves, J.T., Anstey, J.E., Golshani, P., and Portera-Cailliau, C. (2013). Circuit level defects in the developing neocortex of Fragile X mice. Nat. Neurosci. *16*, 903–909.
4. Berkes, P., Orbán, G., Lengyel, M., and Fiser, J. (2011). Spontaneous cortical activity reveals hallmarks of an optimal internal model of the environment. Science *331*, 83–87.

5. Kenet, T., Bibitchkov, D., Tsodyks, M., Grinvald, A., and Arieli, A. (2003). Spontaneously emerging cortical representations of visual attributes. Nature *425*, 954–956.
6. Miller, J.E., Ayzenshtat, I., Carrillo-Reid, L., and Yuste, R. (2014). Visual stimuli recruit intrinsically generated cortical ensembles. Proc. Natl. Acad. Sci. USA *111*, E4053–E4061.
7. Ackman, J.B., Burbridge, T.J., and Crair, M.C. (2012). Retinal waves coordinate patterned activity throughout the developing visual system. Nature *490*, 219–225.
8. Shen, J., and Colonnese, M.T. (2016). Development of activity in the mouse visual cortex. J. Neurosci. *36*, 12259–12275.
9. Gahtan, E., Tanger, P., and Baier, H. (2005). Visual prey capture in larval zebrafish is controlled by identified reticulospinal neurons downstream of the tectum. J. Neurosci. *25*, 9294–9303.
10. Zhang, R.W., Li, X.Q., Kawakami, K., and Du, J.L. (2016). Stereotyped initiation of retinal waves by bipolar cells via presynaptic NMDA autoreceptors. Nat. Commun. *7*, 12650.
11. Romano, S.A., Pietri, T., Pérez-Schuster, V., Jouary, A., Haudrechy, M., and Sumbre, G. (2015). Spontaneous neuronal network dynamics reveal circuit's functional adaptations for behavior. Neuron *85*, 1070–1085.
12. Newman, M.E.J., and Reinert, G. (2016). Estimating the number of communities in a network. Phys. Rev. Lett. *117*, 078301.
13. von Luxburg, U. (2007). A tutorial on spectral clustering. Stat. Comput. *17*, 395–416.
14. Hübener, M., and Bonhoeffer, T. (2014). Neuronal plasticity: beyond the critical period. Cell *159*, 727–737.
15. Rauschecker, J.P. (1991). Mechanisms of visual plasticity: Hebb synapses, NMDA receptors, and beyond. Physiol. Rev. *71*, 587–615.
16. Niell, C.M., and Smith, S.J. (2005). Functional imaging reveals rapid development of visual response properties in the zebrafish tectum. Neuron *45*, 941–951.
17. Del Bene, F., Wyart, C., Robles, E., Tran, A., Looger, L., Scott, E.K., Isacoff, E.Y., and Baier, H. (2010). Filtering of visual information in the tectum by an identified neural circuit. Science *330*, 669–673.
18. Preuss, S.J., Trivedi, C.A., vom Berg-Maurer, C.M., Ryu, S., and Bollmann, J.H. (2014). Classification of object size in retinotectal microcircuits. Curr. Biol. *24*, 2376–2385.
19. Dunn, T.W., Gebhardt, C., Naumann, E.A., Riegler, C., Ahrens, M.B., Engert, F., and Del Bene, F. (2016). Neural circuits underlying visually evoked escapes in larval zebrafish. Neuron *89*, 613–628.
20. Scott, E.K., and Baier, H. (2009). The cellular architecture of the larval zebrafish tectum, as revealed by gal4 enhancer trap lines. Front. Neural Circuits *3*, 13.
21. Nevin, L.M., Robles, E., Baier, H., and Scott, E.K. (2010). Focusing on optic tectum circuitry through the lens of genetics. BMC Biol. *8*, 126.
22. Bollobás, B. (1998). Modern Graph Theory (Springer).
23. Barabási, A.L., and Oltvai, Z.N. (2004). Network biology: understanding the cell's functional organization. Nat. Rev. Genet. *5*, 101–113.
24. Girvan, M., and Newman, M.E.J. (2002). Community structure in social and biological networks. Proc. Natl. Acad. Sci. USA *99*, 7821–7826.
25. Watts, D.J., and Strogatz, S.H. (1998). Collective dynamics of 'small-world' networks. Nature *393*, 440–442.
26. Karrer, B., and Newman, M.E.J. (2011). Stochastic block models and community structure in networks. Phys. Rev. E Stat. Nonlin. Soft Matter Phys. *83*, 016107.
27. Shi, J., and Malik, J. (2000). Normalized cuts and image segmentation. IEEE Trans. Pattern Anal. Mach. Intell. *22*, 888–905.
28. Lopes-dos-Santos, V., Conde-Ocazionez, S., Nicolelis, M.A.L., Ribeiro, S.T., and Tort, A.B.L. (2011). Neuronal assembly detection and cell membership specification by principal component analysis. PLoS ONE *6*, e20996.
29. Lopes-dos-Santos, V., Ribeiro, S., and Tort, A.B.L. (2013). Detecting cell assemblies in large neuronal populations. J. Neurosci. Methods *220*, 149–166.
30. Russo, E., and Durstewitz, D. (2017). Cell assemblies at multiple time scales with arbitrary lag constellations. eLife *6*, 19428.
31. Battista, G.D., Eades, P., Tamassia, R., and Tollis, I.G. (1998). Graph Drawing: Algorithms for the Visualization of Graphs, First Edition (Prentice Hall PTR).
32. Wong, R.O.L. (1999). Retinal waves and visual system development. Annu. Rev. Neurosci. *22*, 29–47.
33. Huberman, A.D., Feller, M.B., and Chapman, B. (2008). Mechanisms underlying development of visual maps and receptive fields. Annu. Rev. Neurosci. *31*, 479–509.
34. Blankenship, A.G., and Feller, M.B. (2010). Mechanisms underlying spontaneous patterned activity in developing neural circuits. Nat. Rev. Neurosci. *11*, 18–29.
35. Arroyo, D.A., and Feller, M.B. (2016). Spatiotemporal features of retinal waves instruct the wiring of the visual circuitry. Front. Neural Circuits *10*, 54.
36. Lowe, A.S., Nikolaou, N., Hunter, P.R., Thompson, I.D., and Meyer, M.P. (2013). A systems-based dissection of retinal inputs to the zebrafish tectum reveals different rules for different functional classes during development. J. Neurosci. *33*, 13946–13956.
37. Kita, E.M., Scott, E.K., and Goodhill, G.J. (2015). Topographic wiring of the retinotectal connection in zebrafish. Dev. Neurobiol. *75*, 542–556.
38. Kita, E.M., Scott, E.K., and Goodhill, G.J. (2015). The influence of activity on axon pathfinding in the optic tectum. Dev. Neurobiol. *75*, 608–620.
39. Meyer, M.P., and Smith, S.J. (2006). Evidence from in vivo imaging that synaptogenesis guides the growth and branching of axonal arbors by two distinct mechanisms. J. Neurosci. *26*, 3604–3614.
40. Niell, C.M., Meyer, M.P., and Smith, S.J. (2004). In vivo imaging of synapse formation on a growing dendritic arbor. Nat. Neurosci. *7*, 254–260.
41. Khakhalin, A.S., Koren, D., Gu, J., Xu, H., and Aizenman, C.D. (2014). Excitation and inhibition in recurrent networks mediate collision avoidance in Xenopus tadpoles. Eur. J. Neurosci. *40*, 2948–2962.
42. Pratt, K.G., Dong, W., and Aizenman, C.D. (2008). Development and spike timing-dependent plasticity of recurrent excitation in the Xenopus optic tectum. Nat. Neurosci. *11*, 467–475.
43. Xu, H., Khakhalin, A.S., Nurmikko, A.V., and Aizenman, C.D. (2011). Visual experience-dependent maturation of correlated neuronal activity patterns in a developing visual system. J. Neurosci. *31*, 8025–8036.
44. Ciarleglio, C.M., Khakhalin, A.S., Wang, A.F., Constantino, A.C., Yip, S.P., and Aizenman, C.D. (2015). Multivariate analysis of electrophysiological diversity of Xenopus visual neurons during development and plasticity. eLife *4*, e11351.
45. Zhang, M., Liu, Y., Wang, S.Z., Zhong, W., Liu, B.H., and Tao, H.W. (2011). Functional elimination of excitatory feedforward inputs underlies developmental refinement of visual receptive fields in zebrafish. J. Neurosci. *31*, 5460–5469.
46. Easter, S.S., Jr., and Nicola, G.N. (1997). The development of eye movements in the zebrafish (Danio rerio). Dev. Psychobiol. *31*, 267–276.
47. Hua, J.Y., and Smith, S.J. (2004). Neural activity and the dynamics of central nervous system development. Nat. Neurosci. *7*, 327–332.
48. Nevin, L.M., Taylor, M.R., and Baier, H. (2008). Hardwiring of fine synaptic layers in the zebrafish visual pathway. Neural Dev. *3*, 36.
49. Ramdya, P., and Engert, F. (2008). Emergence of binocular functional properties in a monocular neural circuit. Nat. Neurosci. *11*, 1083–1090.
50. Engert, F., Tao, H.W., Zhang, L.I., and Poo, M.M. (2002). Moving visual stimuli rapidly induce direction sensitivity of developing tectal neurons. Nature *419*, 470–475.
51. Albert, M.V., Schnabel, A., and Field, D.J. (2008). Innate visual learning through spontaneous activity patterns. PLoS Comput. Biol. *4*, e1000137.

52. Sharpee, T.O., Sugihara, H., Kurgansky, A.V., Rebrik, S.P., Stryker, M.P., and Miller, K.D. (2006). Adaptive filtering enhances information transmission in visual cortex. Nature *439*, 936–942.

53. Rochefort, N.L., Garaschuk, O., Milos, R.I., Narushima, M., Marandi, N., Pichler, B., Kovalchuk, Y., and Konnerth, A. (2009). Sparsification of neuronal activity in the visual cortex at eye-opening. Proc. Natl. Acad. Sci. USA *106*, 15049–15054.

54. Pietri, T., Romano, S.A., Pérez-Schuster, V., Boulanger-Weill, J., Candat, V., and Sumbre, G. (2017). The emergence of the spatial structure of tectal spontaneous activity is independent of visual inputs. Cell Rep. *19*, 939–948.

55. Levelt, C.N., and Hübener, M. (2012). Critical-period plasticity in the visual cortex. Annu. Rev. Neurosci. *35*, 309–330.

56. Hensch, T.K. (2005). Critical period plasticity in local cortical circuits. Nat. Rev. Neurosci. *6*, 877–888.

57. Vladimirov, N., Mu, Y., Kawashima, T., Bennett, D.V., Yang, C.T., Looger, L.L., Keller, P.J., Freeman, J., and Ahrens, M.B. (2014). Light-sheet functional imaging in fictively behaving zebrafish. Nat. Methods *11*, 883–884.

58. Westerfield, M. (1995). The Zebrafish Book: A Guide for the Laboratory Use of Zebrafish (Brachy- danio rerio) (University of Oregon Press).

59. Ahrens, M.B., Li, J.M., Orger, M.B., Robson, D.N., Schier, A.F., Engert, F., and Portugues, R. (2012). Brain-wide neuronal dynamics during motor adaptation in zebrafish. Nature *485*, 471–477.

60. Golshani, P., Gonçalves, J.T., Khoshkhoo, S., Mostany, R., Smirnakis, S., and Portera-Cailliau, C. (2009). Internally mediated developmental desynchronization of neocortical network activity. J. Neurosci. *29*, 10890–10899.

61. Goldenberg, A., Zheng, A.X., Fienberg, S.E., and Airoldi, E.M. (2010). A survey of statistical network models. Found. Trends Mach. Learn. *2*, 129–233.

62. Chen, Z., Li, X., and Desplan, C. (2012). Deterministic or stochastic choices in retinal neuron specification. Neuron *75*, 739–742.

63. Goldberg, M.K., Hayvanovych, M., and Magdon-Ismail, M. (2010). Measuring similarity between sets of overlapping clusters. In Proceedings of the 2010 IEEE Second International Conference on Social Computing (IEEE), pp. 303–308.

STAR★METHODS

KEY RESOURCES TABLE

REAGENT or RESOURCE	SOURCE	IDENTIFIER
Chemicals, Peptides, and Recombinant Proteins		
SeaPlaque Agarose	Lonza	Cat. No. 50101
Experimental Models: Organisms/Strains		
Zebrafish: Tg(elavl3:H2B- GCaMP6s)	[57]	RRID: ZFIN Tg insertion jf5Tg
Software and Algorithms		
MATLAB 2014b, 2015b (Data analysis)	MathWorks	http://www.mathworks.com
Zen Black 2012 Service Pack 2 (Image acquisition)	Carl Zeiss Pty Ltd	http://www.zeiss.com

CONTACT FOR REAGENT AND RESOURCE SHARING

Further information and requests for resources and reagents should be directed to and will be fulfilled by the Lead Contact, Geoffrey Goodhill (g.goodhill@uq.edu.au).

EXPERIMENTAL MODEL AND SUBJECT DETAILS

Zebrafish

All procedures were performed with approval from The University of Queensland Animal Ethics Committee. Nacre zebrafish (*Danio rerio*) embryos expressing *elavl3:H2B-GCaMP6s*, of either sex, were collected and raised according to established procedures [58] and kept under a 14/10 hr on/off light cycle except where otherwise indicated. Larvae were fed live rotifers (*Brachionus plicatilis*) from 5 dpf unless otherwise indicated.

METHOD DETAILS

Dark rearing (DR)

Larvae were placed, at 5–8 hpf, into 35 mm petri dishes with E3 medium [58] (in mM): 5 NaCl, 0.17 KCl, 0.33 $CaCl_2$, 0.33 $MgCl_2$ (pH 7.2), in a dark box, in a dark incubator at 28.5 degrees, in a dark room until 6 dpf. They were then embedded in 2% low melting point agarose (Lonza) in a 35 mm petri dish, and overlaid with E3 medium prior to 2-photon imaging.

Enucleations at 24 hpf

Larvae at 23–25 hpf were anesthetized with 0.2 mM tricaine in E3 and embedded in 2% low melting point agarose. A sharpened tungsten needle was used to remove one eye or both eyes. The larvae were allowed to recover for 1 hr and then removed from the agarose and reared normally on a 14/10 hr light cycle.

Featureless-rearing (FR)

Each larva was placed, at 5–24 hpf, alone into 4 cm diameter hollow light bulbs, with all labels and interior filament removed. The bulb exteriors were painted white, filled with E3 and plugged with white cotton wool. The larvae were raised until 6 dpf in 28.5 degrees and 14/10 hr light cycle.

Feeding assay

Individual fish from the two groups (DR or FR) and their respective siblings (NR) were placed (singly) into 35 mm diameter petri dishes containing E3 with 50 *Paramecia* (*Paramecium caudatum*) and left for 2 hr. The fish were then removed and pooled back into their respective group. The *Paramecia* remaining in each dish were counted. The identity of a fish as either DR, FR or NR was blinded to the person counting.

2-photon calcium imaging

Zebrafish larvae were embedded in 2% low-melting point agarose in E3 embryo medium in 35 mm diameter plastic petri dishes and the agarose was overlaid with E3. Calcium imaging was performed on two independent imaging systems at a depth of 60 μm from the dorsal surface of the tectal midline. For normal and dark-reared fish (Figures 1, 2, 3, and 5), time-lapse 2-photon images were acquired using a Zeiss LSM 710 upright system with a Chameleon multiphoton imaging laser (Coherent) at an excitation wavelength

of 940 nm. The emitted light was bandpass filtered (500–550 nm) and detected with a nondescanned detector and a 40X/1.0 water-dipping objective (Zeiss). Time-lapse images (400 × 300 pixels) were obtained at 2.2 Hz for 60 min. For enucleated, featureless-reared, and a group of control normal-reared 6 dpf fish (Figures 4 and 6) images were acquired on a separate Zeiss LSM 710 inverted 2-photon microscope. A custom-made inverter tube composed of a pair of beam-steering mirrors and two identical 60 mm focal length lenses arranged in a 4f configuration was used to allow imaging with a 40X/1.0 NA water-dipping objective (Zeiss) in an upright configuration. Samples were excited via a Spectra-Physics Mai TaiDeepSee Ti:Sapphire laser (Spectra-Physics) at an excitation wavelength of 940 nm. Laser power at the sample plane was matched between systems (9–12 mW) by measuring the average laser power at 940 nm using a compact power meter (PM100A, Thorlabs). The emitted light was bandpass filtered (500–550 nm) and detected with a nondescanned detector. Time-lapse images (400 × 300 pixels) were obtained at 2.2 Hz for 60 min. Comparisons between fish presented in the text are always between fish imaged on the same microscope.

Image registration

Recordings which showed a drift in the z-plane were discarded. All fluorescence data stacks were corrected for x-y drifts using custom MATLAB software. A 1 hr movie was divided into 6 movies of 10 min each for image processing and then rejoined back for analysis. Frames of a 10 min movie were first aligned with a reference frame within the movie using custom MATLAB software based on MATLAB's rigid image registration algorithm. To align stacks between 10 min movies, reference frames were aligned with the first movie's reference frame.

Cell detection and calcium signals

Custom MATLAB software was used to automatically detect the region-of-interest (ROI) of each active cell, i.e., the group of pixels defining each cell. The software searched for active pixels, i.e., pixels that showed changes in brightness across frames, resulting in an activity heatmap of all the active regions across frames [59]. The activity map was then segmented into regions using a watershed algorithm, with a similar threshold applied to all movies. Within each segmented region, we computed correlation coefficients of all pixels in the region with the mean of the most active pixel and its eight neighboring pixels. Correlation coefficients showed a bimodal distribution; one peak of highly correlated pixels representing pixels of the cell within the region, and a second peak of relatively low correlation coefficients representing nearby pixels within the region which were not part of the cell. Using a Gaussian mixture model, we found the threshold correlation which differentiated between pixels likely to form the active cell and neighboring pixels that were not part of the cell. We also required that each detected active area covered at least 26 pixels (5.5 μm^2). The software allowed visual inspection and modification of the parameter values where needed. All pixels assigned to a given cell were averaged to give a raw fluorescence trace over time. Raw calcium signals for each cell, $F(t)$, were then converted to represent changes from baseline level, $\Delta F/F(t)$ defined as $(F(t) - F_0(t))/F_0(t)$. The time varying baseline fluorescence, $F_0(t)$, for each cell was a smoothed curve fitted to the lower 20% of the points. $F_0(t)$ was the minimum of the smoothed fluorescence trace in a 3 s window centered at t.

Calcium events

We defined an event as a major deflection in fluorescence levels from baseline, indicating an increase in firing rate of a neuron. For each neuron, each time bin in which its amplitude was two standard deviations above the mean was marked with a 1. This provided us with a binary activity matrix where each row represents a neuron and each column represents a time bin. This matrix was used for subsequent calculations.

To quantify event frequency all local maxima which were both above two standard deviations above the neuron's mean and at least 0.5 $\Delta F/F(t)$ different in amplitude from the immediately neighboring maxima were selected.

Determination of a statistically significant level of co-activity

To establish a threshold for the significance for the number of co-active neurons, the binary activity matrix was randomly shuffled 500 times within neurons, keeping the number of events per cell identical, but changing their timing. The threshold corresponding to a significance level of $p < 0.05$ was estimated as the number of activated neurons in a single frame that exceeded 5% of these surrogate datasets. When determining significant frames for further assembly detection we considered coactivity levels in the PVL neurons only.

Significance of pairwise correlation coefficients

We computed the pairwise correlation coefficient r between all pairs of neurons, to give a distribution $P(r)$. To assess statistical significance we temporally displaced each neuron's calcium trace randomly with respect to the other traces using a SHIFT algorithm as described previously [60], disrupting the temporal relationship between neurons while preserving the temporal structure within each neuron (such as event frequency, event decay time and noise level). We then calculated the correlation coefficient between all pairs of shifted traces to obtain a null distribution. Pairs of neurons with a correlation coefficient greater than the 95th percentile of correlation coefficients in the null distribution were deemed statistically significant ($p < 0.05$).

Estimating the number of communities in the graph

To estimate the number of communities present in a given graph we applied a recently introduced approach which is based on statistical inference methods [12]. This approach aims to fit a generative model of a graph, which is capable of exhibiting community

structure, to an observed graph, in order to infer information about the community structure from the parameters of the fitted model. As a generative model we used the degree-corrected stochastic block model [12, 26]. In this model, given a number of nodes and a number of communities k, every node is independently assigned to one of k communities. Edges are then drawn independently depending on degree as well as the corresponding community of the nodes. Provided that edges between nodes of the same community are drawn with a higher probability than edges between different communities the resulting graph will exhibit community structure. Unlike the classical stochastic block model [61], which fails to adequately capture variable degree distribution, the degree-corrected stochastic block model is able to fit any graph [26]. Within this model it is possible to derive an explicit expression for the probability of having k communities and a community assignment g given the actual observed graph G, $\Pr[k, g|G]$. Using numerical integration the probability of having k communities given the actual observed graph G, $\Pr[k|G]$ can be obtained as an approximation $\Pr[k, g|G] \approx (1/N)\sum_{n=1}^{N}\delta_{k,k^{(n)}}$ by sampling a sequence of points $\{(k^{(n)}, g^{(n)})\}_{1\leq n\leq N}$ from the joint distribution using a Markov Chain Monte Carlo procedure. This provides an estimate for the number of communities in the observed graph in terms of a probability distribution. From this distribution we inferred the most likely number of communities present in the graph. We implemented the sampling algorithm in MATLAB based on the original implementation obtained from http://www.umich.edu/~mejn/communities/communities.zip.

Community structure assignment

Given the number of communities determined above, for the actual clustering we used spectral clustering methods. These approximately solve particular graph cutting objectives efficiently by looking at spectral properties of different graph Laplacians [13]. We clustered the graphs according to the Ncut objective, which aims to find clusters such that the number of edges between clusters is minimized, while the number of edges within each cluster is maximized [27].

Assembly detection

Given the set of frames with significant PVL neuronal activity patterns in the form of binary vectors, $\{x\}$, we constructed a graph taking these frames as the underlying set of nodes. Edges between the nodes were drawn depending on the similarity of the corresponding activity patterns according to the cosine distance, $d_{\text{cosine}} : (x, x') \mapsto 1 - \langle x, x'\rangle / (\|x\| \, \|x'\|)$ (Figure 4B). More precisely, we constructed this graph as an unweighted k-nearest-neighbor graph with k chosen to be equal to $\ln|\{x\}|$ [13], increasing k if the network turned out to be disconnected. In such a graph, community structure corresponds to similar patterns of neuronal activity, and therefore also to the neuronal assemblies of co-active neurons. We then took the corresponding frames of similar activity patterns and averaged them so that we obtained a set of initial core assembly activity patterns $\{\tilde{\alpha}\}$, discarding neurons with less than 20% affinity to the assembly. We used these preliminary core assembly activity patterns in order to refine the clustering of the whole set of frames, motivated by preliminary results using surrogate data. First we disregarded any core assembly activity pattern which corresponded to and originated from a particularly small group of frames. In particular, given the size of all the groups we set the threshold to 1.5 standard deviations below the mean, provided that the size of the group already exceeded 4 frames. We then combined groups whose corresponding core assembly activity patterns were similar, in the sense that $\min((\langle\tilde{\alpha}', \tilde{\alpha}\rangle/\|\tilde{\alpha}\|^2), (\langle\tilde{\alpha}, \tilde{\alpha}'\rangle/\|\tilde{\alpha}'\|^2)) > 2/3$ for $\tilde{\alpha}$ and $\tilde{\alpha}'$ two distinct core assembly activity patterns in their binary form. This similarity condition ensured that the overlap of the two activity patterns relative to their absolute level of activity was comparable. We did this recursively, and from these rearranged groups defined a new set of core assembly activity patterns. These were then used to re-assign all the activity patterns under consideration into a new set of groups. For an activity pattern x to be assigned to a group defined by a core assembly activity pattern $\tilde{\alpha}$ we required them to be similar enough to one another in the sense that the conditions $(\langle\tilde{\alpha}, x\rangle/\|x\|^2) > 1/2$ and $(\|x\|^2/\|\tilde{\alpha}\|^2) > 1/2$ were satisfied. This ensured that the overlap of the activity pattern with the core assembly activity pattern relative to its absolute activity level, as well as the activity pattern's absolute activity level relative to the core assembly activity pattern's absolute activity level, exceeded 0.5. If these conditions were satisfied we assigned the activity pattern to the core assembly activity pattern's group which was closest in the cosine distance, and otherwise rejected it. We thus obtained groups of highly similar activity patterns. Averaging the activity patterns for every group, and imposing a threshold of 20% affinity on the resulting pattern, we obtained a final set of core assembly activity patterns $\{\alpha\}$, and the assemblies as the neurons whose affinity exceeded the threshold in the corresponding pattern. As before, we neglected groups smaller than 1.5 standard deviations below the mean size of groups provided that the size already exceeded 4 frames.

Evaluating the performance of assembly detection

In order to evaluate the performance of our proposed algorithm for detection of assemblies and to test it against an established method based on an independent-component-analysis approach [29], we generated 1567 surrogate datasets based on 394 different predefined assembly configurations at 4 different levels of assembly occurrence frequency.

Each dataset consisted of 5 assemblies generated on a 12 × 12 grid of neurons. Each assembly center was chosen randomly in this grid. 48 random samples were then drawn from a Gaussian function with that center, and all grid positions within which at least one sample fell were deemed to represent active neurons. Given two assemblies a and a′, in the sense of index sets of the corresponding patterns, generated in this way, the pairwise overlap was measured as $(a, a') \mapsto (|a \cap a'| / \min(|a|, |a'|))$. The mean pairwise overlap for each dataset of 5 assemblies was defined as the average of all pairwise overlaps between assemblies. From a large number of such datasets, we sampled a subset such that the mean pairwise overlap of the corresponding assembly configurations was approximately uniformly distributed in the range from 0.0 to roughly 0.6.

Surrogate calcium activity movies for each dataset of duration 1 hr were then created as follows. Neurons were modeled as Poisson processes [28], each with a different baseline firing rate drawn from a discrete uniform distribution $R \sim U[1,6]$ Hz. Assembly activation was modeled as a synchronous increase in the firing rate of assembly neurons [28]. For each assembly, a proportion q of time bins (q = 0.125%, 0.2%, 0.375%, 0.5%) was selected to be assembly activation bins, in which assembly neurons elevated their firing rate from their baseline by a gain factor of 6. To maintain the same firing rate across all neurons, each non-assembly neuron also elevated its firing rate by the same gain factor in the same proportion of bins (q) which were selected randomly for each neuron. After producing Poisson spiking from this population rate matrix, the activity for each cell was convolved with a calcium kernel with a 2 s half decay time [62] to generate surrogate calcium signals. These were then processed in the same way as experimental calcium signals for input to the assembly detection algorithm. To measure the performance of detection of surrogate assemblies we used a Best Match score, defined as $1 - 1/(|\mathbb{A}| + |\mathbb{A}'|)(\sum_{a\in\mathbb{A}} \min_{a'\in\mathbb{A}'} d(a,a') + \sum_{a'\in\mathbb{A}'} \min_{a\in\mathbb{A}} d(a',a))$ with $d : (a,a') \mapsto 1 - (|a \cap a'| / |a \cup a'|)$ for two assembly configurations $\mathbb{A}$ and $\mathbb{A}'$. This is a specific application of a general method for determining the degree of similarity of two different clusterings of the same data [63]. If the original $\mathbb{A}$ and reconstructed $\mathbb{A}'$ sets of assemblies exactly coincide their Best Match score is 1, and if there is no overlap their score is 0.

QUANTIFICATION AND STATISTICAL ANALYSIS

Statistical correction for multiple comparisons

To correct for multiple comparisons we used Bonferroni or Benjamini Hochberg correction. p values quoted in the text are already adjusted, where appropriate, according to these corrections.

DATA AND SOFTWARE AVAILABILITY

Software

Data analysis was coded in MATLAB. The codes will be made available upon request.